 doi:10.20944/preprints202002.0216.v1

Article

In-stream Energy by Tidal and Wind-driven Currents: An Analysis for the Gulf of California

Vanesa Magar [1,†,*], Victor M. Godínez [1,†], Markus S. Gross[1], Manuel López-Mariscal[1], Anahí Bermúdez-Romero[1], J. Candela[1] and L. Zamudio [2]

1 Physical Oceanography Department, CICESE, Carretera Ensenada-Tijuana No. 3918, Zona Playitas, Ensenada C.P. 22860, Baja California, Mexico
2 Center for Ocean-Atmospheric Prediction Studies, Florida State University, Tallahassee, FL 32306-2840
* Correspondence: vmagar@cicese.edu.mx; Tel: +52-1646-175-0500
† These authors contributed equally to this work.

Abstract: We analyzed the peak spring tidal current speeds, annual mean tidal power densities (TPD) and annual energy production (AEP) obtained from experiment 06.1, referred as the "HYCOM model" throughout, of the three dimensional (3D), global model HYCOM in an area covering the Baja California Pacific and the Gulf of California. The HYCOM model is forced with astronomical tides and surface winds alone, and therefore is particularly suitable to assess the tidal current and wind-driven current contribution to in-stream energy resources. We find two areas within the Gulf of California, one in the Great Island Region and one in the Upper Gulf of California, where peak spring tidal flows reach speeds of 1.1 meters per s econd. Second to fifth-generation tidal stream devices would be suitable for deployment in these two areas, which are very similar in terms of tidal in-stream energy resources. However, they are also very different in terms of sediment type and range in water depth, posing different challenges for in-stream technologies. The highest mean TPD value when excluding TPDs equal or less than 50 W m^{-2} (corresponding to the minimum velocity threshold for energy production) is of 172.8 W m^{-2}, and is found near the town of San Felipe, at (lat lon) = (31.006 -114.64); here energy would be produced during 39.00% of the time. Finally, wind-driven currents contribute very little to the mean TPD and the total AEP. Therefore, the device, the grid, and any energy storage plans need to take into account the periodic tidal current fluctuations, for optimal exploitation of the resources.

Keywords: Tidal Power Density; In-Stream Renewable Energy; Peak Spring Tide Flow; Annual Energy Production; Gulf of California

1. Introduction

Tides, winds, and density gradients contribute to the generation, the characteristics, and the evolution of ocean currents, but their percentage contribution may vary in space and time. In the open ocean, tidal currents are assumed to play a small role because the water depth is usually large. In contrast, in estuaries, inlets, and marginal seas, the tidal amplitudes and speeds increase due to funnelling and resonance effects caused by the bathymetry and the geometry of the basin. Tidal currents can be identified very easily in *in-situ* measurements or numerical simulations, because the tidal forcing is harmonic with well defined frequencies given by the tidal potential [1]. However, in general it is more complex to separate the residual current into wind-driven and density-driven components. From a renewable energy characterization perspective, there are multiple studies that have assessed water level ranges for tidal barrages or tidal lagoons [2–4], and tidal and marine current speeds for in-stream device deployments [5–8], at different sites around the world.

 doi:10.20944/preprints202002.0216.v1

Most studies focus on one type of energy only, because generally the best sites for energy exploitation do not overlap. Also, the energy conversion devices themselves, together with the necessary infrastructure, may be different. Moreover, from an economic perspective it makes more sense to consider one development at a time, and ensure best return on investment before moving on. However, in some specific cases, assessing a combination of options is the main deliverable of a project [9]. In some other cases, combining technologies is considered financially robust, but most studies conclude that such combinations refer rather to co-location of multiple users rather than co-location of tidal energy technologies [10].

The purpose of this paper is to characterize the tidal currents and wind-driven currents in the Gulf of California, with some comments about tidal resources in the Baja Californian Pacific, and analyze their respective contributions to in-stream renewable energy generation. In Sec. 2, we present the model validations, and evaluate the contribution of the barotropic tidal currents and the wind-driven currents to the mean peak flow speeds, in-stream power density, and annual energy production. In Sec. 3, we describe the HYCOM model configuration used in this work. We also describe the in-situ measurements and the methodology adopted for the verification of the model predictions. In Sec. 4, we close with some concluding remarks.

2. Results and Discussion

The HYCOM model is used to analyse the percentage contributions to Tidal Power Density (TPD) and Annual Energy Production (AEP), of the wind-driven currents and the tidally-driven currents. The analysis is performed over the domain and with the bathymetry shown in Fig. 1. The red markers in the Great Island Region (GIR) correspond to ADCP moorings in the San Lorenzo Channel (SLC), the San Esteban Channel (SEC), the Ballenas Channel (BC). and the Delfin Sill (DS). Another ADCP mooring near Isla San Jorge (ISJ) was also used for verification.

Preprints (www.preprints.org) | NOT PEER-REVIEWED | Posted: 16 February 2020 doi:10.20944/preprints202002.0216.v1

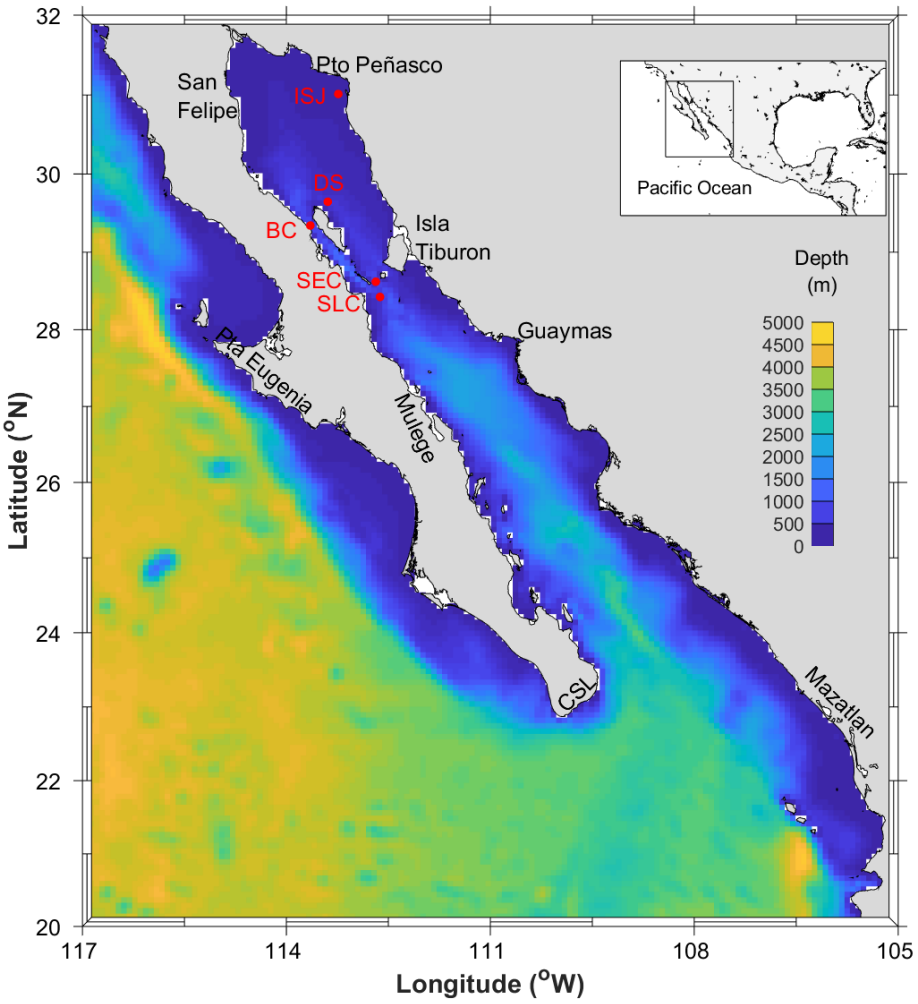

Figure 1. Model domain and bathymetry with markers showing ADCP moorings.

2.1. Verification of model predictions against in-situ measurements

Fig. 2 shows the vertically-integrated flow speed obtained with the HYCOM model (in red) and the measurements (in dashed blue) from the 1^{st} of October to the 16^{th} of October 2011, in the San Esteban Channel (SEC) mooring (shown in Fig. 1). The verification is carried out for the barotropic tidal currents only, and to compare the hourly tidal current time series obtained from the measurements to those from the model, the former had to be reconstructed for the period of simulation of the latter, i.e. for the period between 01/10/2011 01:00:00 and 01/10/2012 00:00:00 - this is explained in more detail in Sec. 3. Table 1 shows the yearly average of the modelled (mod) and measured (obs) values (shown next to each other in "mod/obs" format) of $\overline{U}$ (see Eqn. 1), $\overline{TPD}$ (see Eqn. 2), the AEP (see Eqn. 3), the relative error RE_x (see Eqn. 5) and the $RMSE_x$ (see Eqn. 6) for $x = \overline{U}$ and $x = \overline{TPD}$, as well as the correlation coefficient $\rho_{X,Y}$ (see Eqn. 4), at the five verification sites. In the GIR $\rho_{X,Y}$ is either 0.91 or 0.92, and it is 0.71 at ISJ. $\rho_{X,Y}$ is much lower at ISJ because the bathymetry used by the model in the region of San Jorge Bay is not as good as the bathymetry used in the GIR. Please note that no results of the RE or $RMSE$ for AEP are shown because they are the same as for the TPD.

Preprints (www.preprints.org) | NOT PEER-REVIEWED | Posted: 16 February 2020 doi:10.20944/preprints202002.0216.v1

Table 1. Verification table for mean values.

Units: U $[\mathrm{m\,s^{-1}}]$, TPD $[\mathrm{W\,m^{-2}}]$, AEP $[\mathrm{kWh\,m^{-2}}]$, RE [%], RMSE$_U$ $[\mathrm{m\,s^{-1}}]$, RMSE$_{TPD}$ $[\mathrm{W\,m^{-2}}]$								
Mooring	$\overline{U}$ mod/obs	$\overline{TPD}$ mod/obs	AEP mod/obs	$\rho_{X,Y}$	RE$_U$	RE$_{TPD}$	RMSE$_U$	RMSE$_{TPD}$
ISJ	0.202/0.206	7.56/10.48	66.45/92.07	0.71	2.0%	27.8%	9.1×10^{-2}	14.13
DS	0.182/0.182	7.44/7.67	65.35/67.33	0.92	0.2%	3%	4.8×10^{-2}	6.05
BC	0.190/0.360	8.69/60.60	76.33/532.3	0.92	47%	86%	21×10^{-2}	98.2
SEC	0.372/0.417	56.28/85.24	494.4 / 748.7	0.91	10.8%	34%	11.7×10^{-2}	63.98
SLC	0.263/0.388	21.98/72.75	193.1/639.1	0.92	32.2%	69.8%	17.3×10^{-2}	102.0

The model underestimates $\overline{U}$ and $\overline{TPD}$ at all verification sites. The agreement is significantly worse at BC and at SLC, the two moorings furthest to the west. However, good agreement between model and observations is obtained at DS, ISJ and SEC. We also have significantly worse agreement at BC and at SLC for the annual mean maximum spring tide speeds and TPD, shown in Table 2, but the RE_U and $RMSE_U$ at the other three sites, are less than 10% and less than $3.7 \times 10^{-1}\ \mathrm{m\,s^{-1}}$, respectively.

Table 2. Verification table for mean maximum spring tidal values.

Units: U $[\mathrm{m\,s^{-1}}]$, TPD $[\mathrm{W\,m^{-2}}]$, RMSE$_U$ $[\mathrm{m\,s^{-1}}]$, RMSE$_{TPD}$ $[\mathrm{W\,m^{-2}}]$						
Mooring	$\overline{U}_{STM}$ mod/obs	$\overline{TPD}_{STM}$ mod/obs	RE$_U$	RE$_{TPD}$	RMSE$_U$	RMSE$_{TPD}$
ISJ	0.415/0.459	38.76/55.80	9.8%	30.6 %	11.9×10^{-2}	38.56
DS	0.417/0.399	39.6/35.62	-4.6%	-11.2%	4.5×10^{-2}	12.23
BC	0.467/0.822	54.6/311.1	43.2%	82.5%	36.7×10^{-2}	290.2
SEC	0.866/0.928	347.4 /437.7	6.6%	20.6%	8.3×10^{-2}	119.36
SLC	0.568/0.918	101.7/436.7	38.2%	76.7%	36.8×10^{-2}	390.6

The $RMSE_U$ in Table 2 are of the same order as those reported in Defne *et al.* [7] for their tidal resource characterization study along the coast of Georgia (USA), and although we considered a different study site and we used a different model, this shows that the model predictions are reliable.

Preprints (www.preprints.org) | NOT PEER-REVIEWED | Posted: 16 February 2020 doi:10.20944/preprints202002.0216.v1

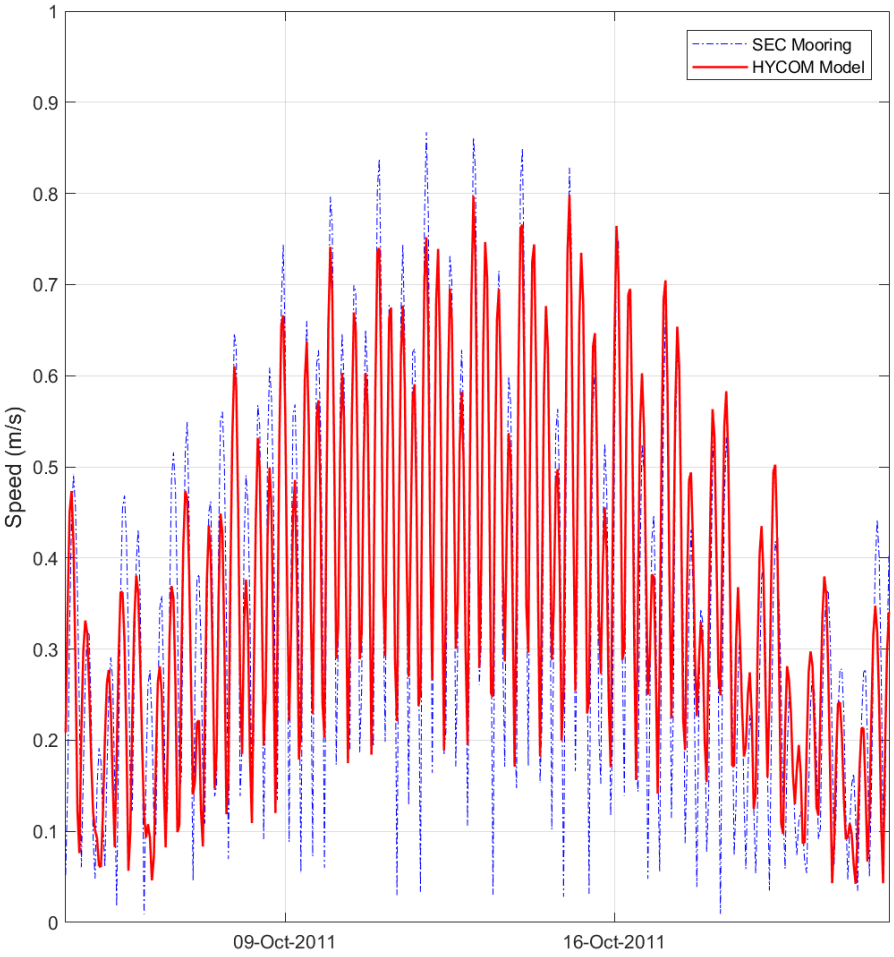

Figure 2. Tidal harmonic reconstruction of the modelled (solid red) and measured (dashed blue) tidal speed $\left[\mathrm{m\,s^{-1}}\right]$ time series at the SEC mooring, for the same two-week period.

2.2. *Analysis of the barotropic tidal signal*

The map of $\overline{U}_{STM}$, the annual mean of the spring tide maxima, is shown in Fig. 4. The map shows two regions with $\overline{U}_{STM}$ values close to 1 m s^{-1}. These two regions define two approximate transects that are shown in Fig. 3.

Preprints (www.preprints.org) | NOT PEER-REVIEWED | Posted: 16 February 2020 doi:10.20944/preprints202002.0216.v1

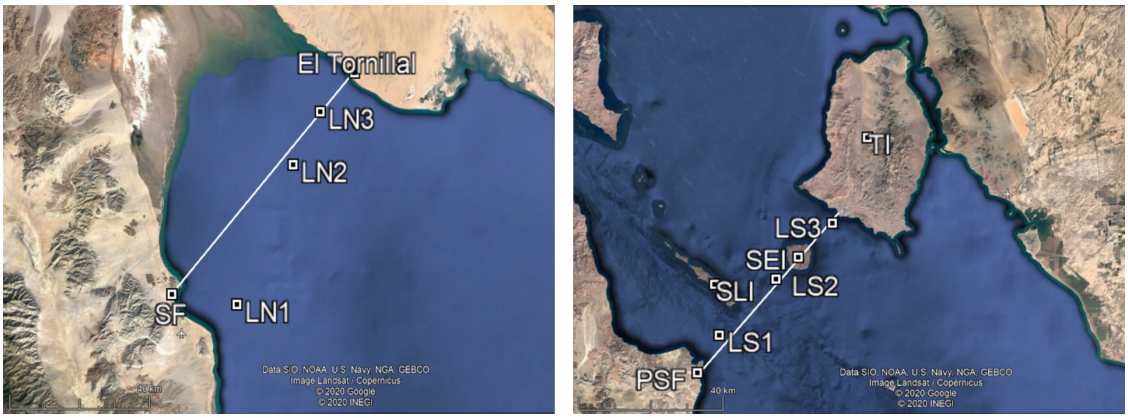

Figure 3. Northern (left) and southern (right) regions with largest tidal current speeds, with geographical markers for: San Felipe (SF), El Tornillal, Punta San Francisquito (PSF), San Lorenzo Island (SLI), San Esteban Island (SEI), and Tiburón Island (TI). The six locations with highest tidal current speeds are also shown.

The first region is in the Upper Gulf of California, in the Colorado River Delta approach in the North, approximately along a transect running between San Felipe (SF) and El Tornillal, shown on the left of Fig. 3. The second region is in the GIR, approximately along a transect joining Punta San Francisquito (PSF) to the western shore of Tiburón Island (TI), shown on the right of Fig. 3. These landmarks are also shown in the first close-up figure, corresponding to Fig. 5. Now, although most tidal stream devices operate at mean spring tidal speeds of 2.5 m s^{-1} or larger, some devices can operate at locations where spring tidal currents are as low as 1.3 m s^{-1} [11,12], and where depths are between 60 m and 120 m. It is possible that such values of $\overline{U}_{STM}$ are reached in the Upper Gulf or in the Great Island Region. The location where the model predicts a maximum of U_{max} is near San Felipe, and this maximum is of 1.11 m s^{-1} (see Table 3), which is not far from the minimum threshold of the GreenDeep device [12]. There are three other location where U_{max} is above one. However, the model used here predicts $\overline{U}_{STM}$ values between 0.8 m s^{-1} and 0.9 m s^{-1}. Tidal energy developers need to design technologies that can exploit lower flow speeds than first generation devices. Higher resolution models need also to be developed in order to characterize the flow speeds with better spatial detail, in particular in the GIR.

Preprints (www.preprints.org) | NOT PEER-REVIEWED | Posted: 16 February 2020 doi:10.20944/preprints202002.0216.v1

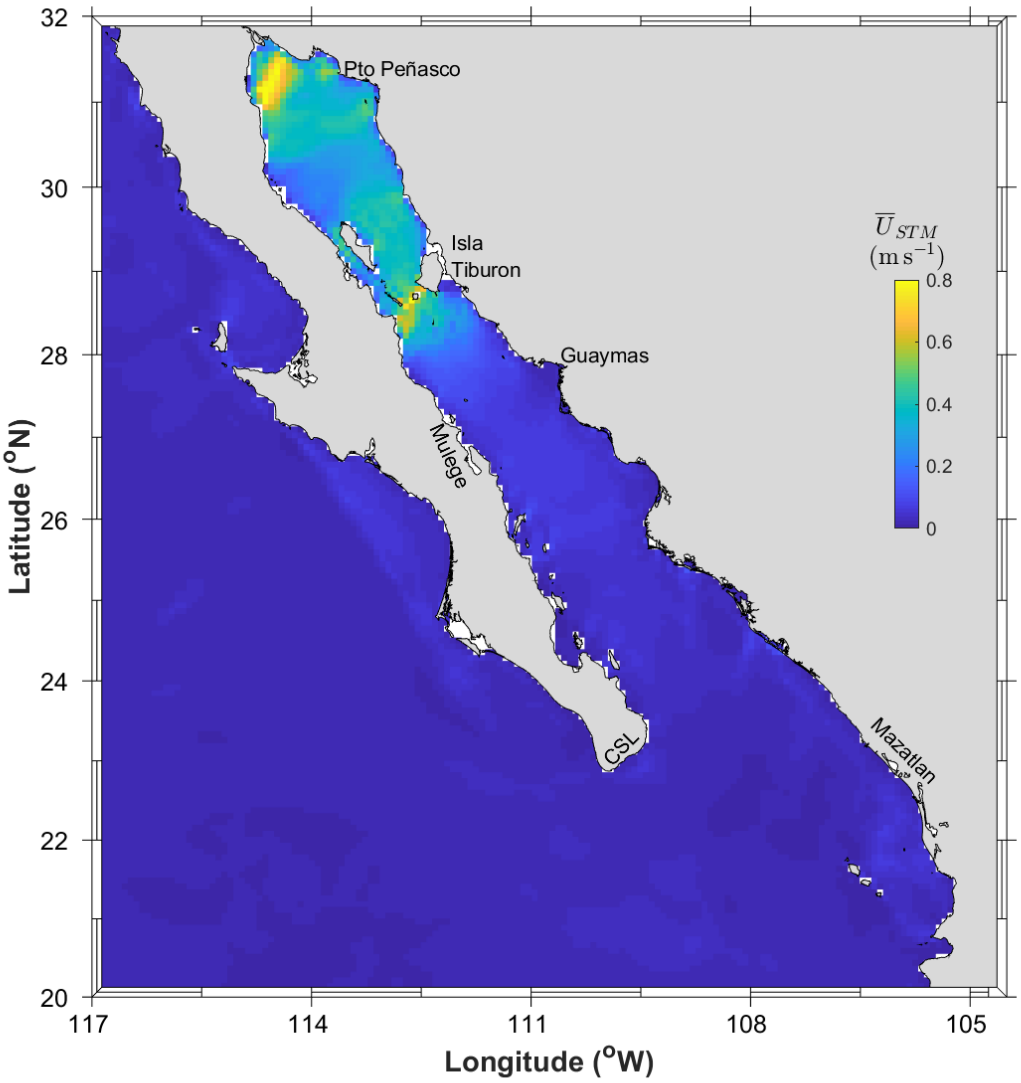

Figure 4. Map of Annual Mean of the Spring Tide Maximum Speed [m s^{-1}].

Figure 5 shows the regions where TPD reaches values above 50 W m^{-2}, and the resulting annual mean of those values, defined as $\overline{TPD_{>50}}$. We chose 50 W m^{-2} because it corresponds to a minimum threshold speed, U_m of 0.46 m s^{-1}, which is roughly the minimum speed at which Tidal Energy Converters (TECs) start reacting to the flow and produce energy. Any speeds below U_m do not contribute to $\overline{TPD}$ or the AEP. This minimum threshold defines the regions with no commercially viable mean tidal power density. Based on the HYCOM model, such non-commercially viable regions appear as blank patches in Fig. 5. The model defines a transect that joins (lat lon) = ($28^\circ N$ $112^\circ 45' 54.5'' W$) in the Peninsula to (lat lon) = ($28^\circ 27' 05.7'' N$ $111^\circ 41' 07.8'' W$) on mainland Sonora, in the Gulf of California. According to the model, any commercially viable regions for tidal energy exploitation in the Gulf of California would be located north of this transect. According to the model as well, except for the Colorado River Delta Approach, there are very few places with water depths below 50 m which are commercially viable. However, as discussed by Magar [13], there are some known exploitable locations in the Channel between Tiburón Island and mainland Sonora. Therefore, the HYCOM model may serve as a guidance to identify some locations with exploitable resources, but has some limitations at shallow water depths, which may only be solved with better bathymetric data, and models with higher resolution. It may be noted that the only location in the

Preprints (www.preprints.org) | NOT PEER-REVIEWED | Posted: 16 February 2020 doi:10.20944/preprints202002.0216.v1

Baja Californian Pacific that may have exploitable tidal energy resources, would be the channel just north of Punta Eugenia (shown in Fig. 5), as the small colored area in the Baja Californian Pacific coast suggests. However, the sites along this coast will not be discussed further in this paper.

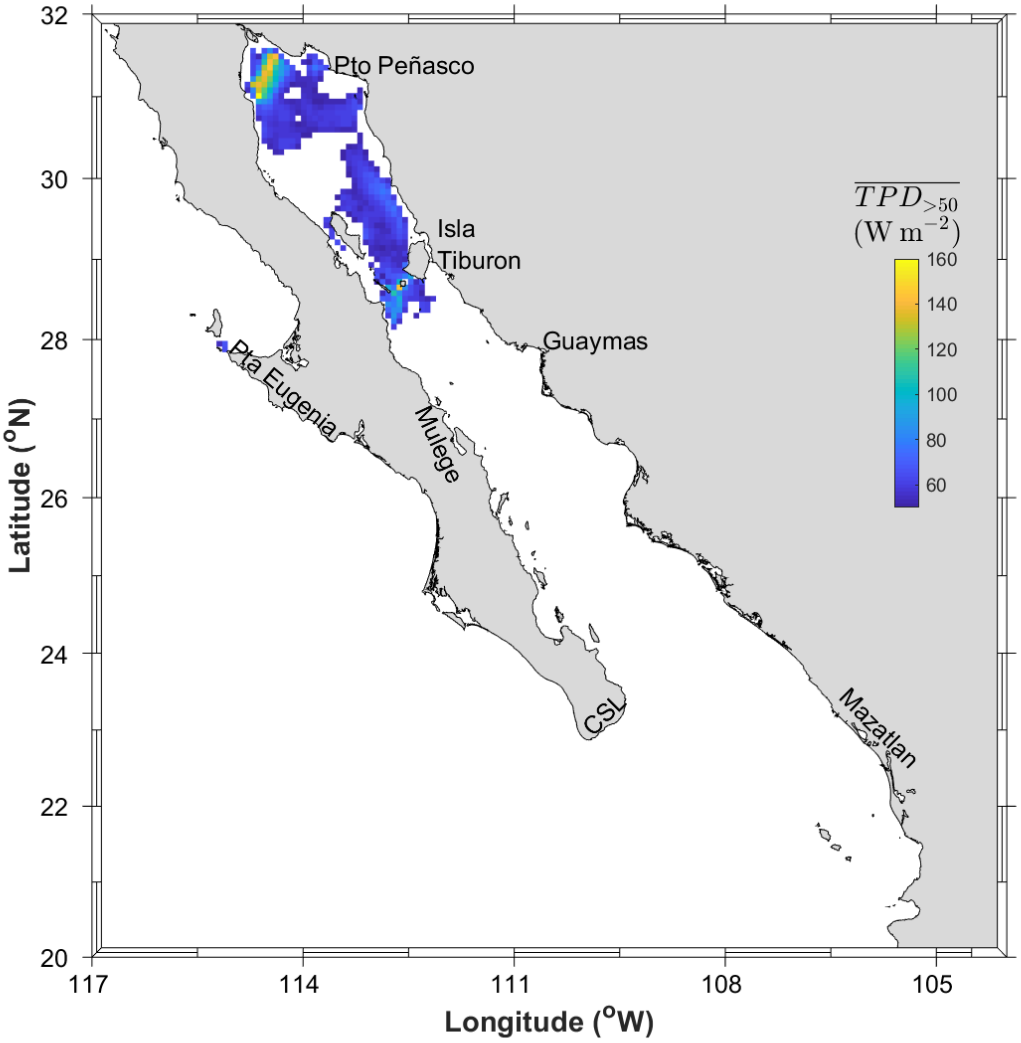

Figure 5. Map of $\overline{TPD_{>50}}$, corresponding to the mean of TPD when $TPD > 50$ W m^{-2}.

Figure 6 shows the percentage time (%T) when $TPD > 50$ W m^{-2}. The best locations in terms of percentage time would correspond to those with largest %T. Along the San Francisquito $-$ Tiburón Island transect (the southern transect), the three most relevant locations are LS1, LS2 and LS3 (ordered from west to east), their details are in Table 3. Along the San Felipe $-$ El Tornillal transect (the northern transect), the three most relevant locations are LN1, LN2 and LN3 (ordered from west to east), their details are summarized in Table 3. These six locations are highlighted as void circles in Fig. 6.

Preprints (www.preprints.org) | NOT PEER-REVIEWED | Posted: 16 February 2020 doi:10.20944/preprints202002.0216.v1

Table 3. Locations with largest six maximal speeds, U_{max}, over the simulation year.

Units: U $\left[\mathrm{m\,s^{-1}}\right]$ and TPD $\left[\mathrm{W\,m^{-2}}\right]$					
Location	(lat lon)	$\overline{U}_{STM}$	$\%T$	$\overline{TPD}_{>50}$	U_{max}
LN1	(31.006 -114.64)	0.899	39.00	172.8	1.11
LN2	(31.348 -114.48)	0.800	33.58	145.1	1.02
LN3	(31.480 -114.40)	0.758	31.1	141.62	1.02
LS1	(28.506 -112.80)	0.733	23.54	106.7	0.89
LS2	(28.646 -112.64)	0.858	33.34	145.1	1.04
LS3	(28.786 -112.48)	0.676	17.30	92.94	0.83

In terms of barotropic mean tidal power density, the two transects that we have identified are very similar, with slightly lower $\overline{TPD}_{>50}$ values in the southern transect compared to the northern one. However, the tidal range, the water depth, and the characteristics of the seafloor are distinctly different. The southern transect changes drastically from very shallow to depths of several hundred meters, has a seafloor composed of sand and rocks [14], and the tidal range is mostly below 2 m (check the tidal charts produced by CICESE for the tidal gauges in the GIR, by consulting: http://predmar.cicese.mx/). In contrast, the northern transect is macrotidal and with water depths mostly below 50 m, with seafloor composed of cohesive and sandy sediments, and a tidal range that can reach around 6 to 7 m [15,16]. The difference in water depths and seabed sediment composition has important implications on the type of TEC that can be installed. In particular, the TEC moorings would need to be designed differently, and a detailed bathymetry would need to be generated in order to find the locations with depths that are appropriate for deployment. This is not in any way a limitation of the sites, but an opportunity for device and device deployment innovation [17], from 2nd (Gen2) to 5th (Gen5) Generation tidal turbine systems [18], and for local scale site characterization studies [19].

Preprints (www.preprints.org) | NOT PEER-REVIEWED | Posted: 16 February 2020 doi:10.20944/preprints202002.0216.v1

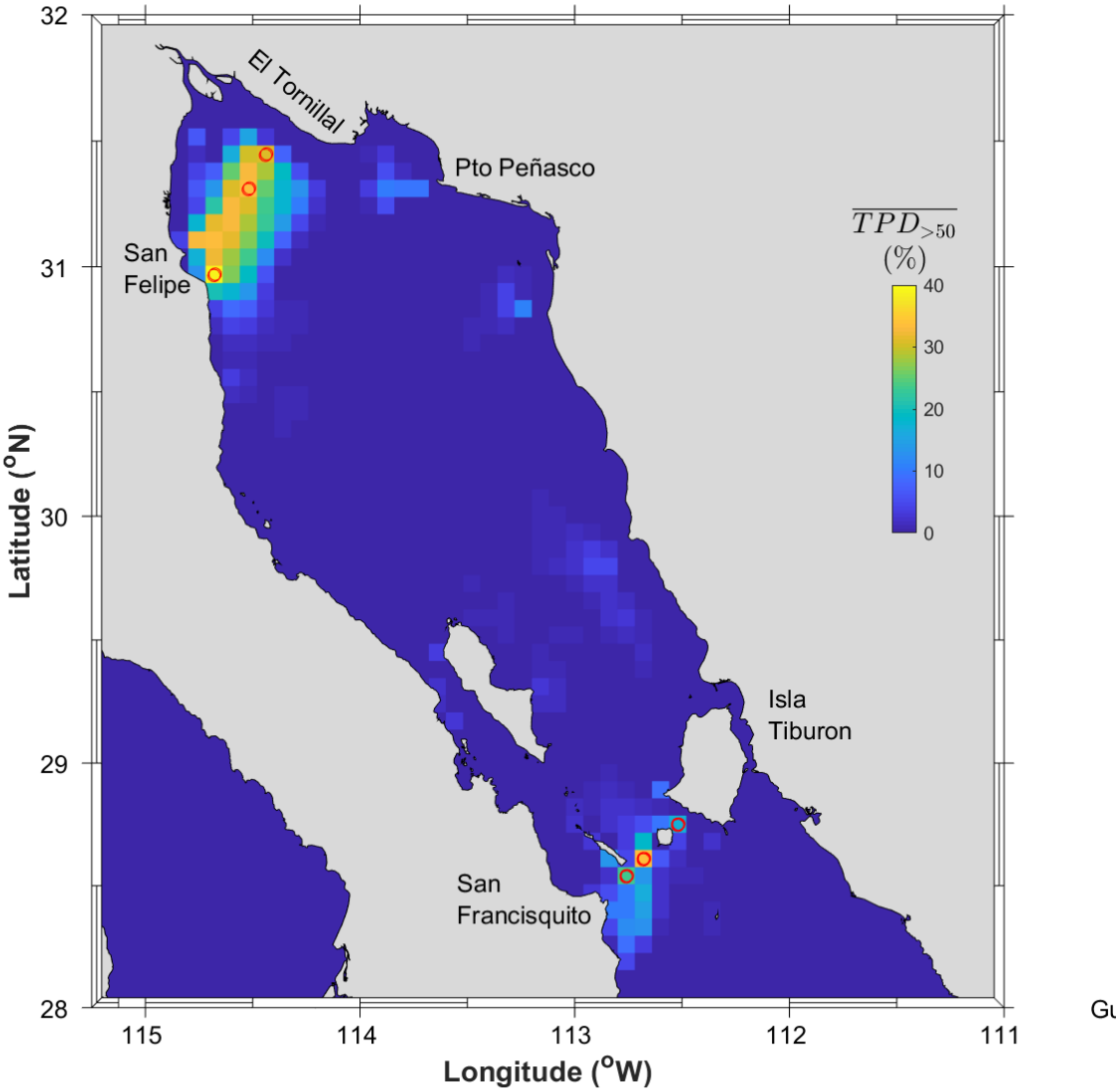

Figure 6. Map of percentage time $\%T$ when $TPD > 50$ W m^{-2}. The red circles correspond to the six most energetic locations, defined in the text.

Figure 6 shows the percentage time, $\%T$, when the barotropic TPD is above 50 W m^{-2}, within the Gulf of California and for latitudes above the 28° parallel. The two transects that have been discussed previously stand out significantly in Fig. 6, in particular the locations along these transects with $\overline{TPD_{>50}}$ above 140 W m^{-2}. The most energetic cells are LN1 near San Felipe in the northern transect, where $\overline{TPD_{>50}} = 172.8$ W m^{-2}, and LS2 and LN2, where $\overline{TPD_{>50}} = 145.1$ W m^{-2}. LS2 is between San Esteban Island (SEI) and San Lorenzo Island (SLI) - shown on the left of Fig. 3, and LN2 is approximately midway between San Felipe and El Tornillal, in the Upper Gulf – shown on the right of Fig. 3. At these three locations, the $\%T$ when $TPD > 50$ W m^{-2} is above to 30%.

Figure 7 shows the tidal AEP when considering only values of TPD above 50 W m^{-2}. In the regions where production is largest (in the region closest to San Felipe), we reach AEP values of 592 kWh m^{-2} yr^{-1}. One tidal stream device with a cross-section diameter of 20 m, or a cross-sectional area of $A = 314.16$ m^2,and an efficiency C_p of 0.35 [20,21], would produce a technical AEP of around 65 MWh yr^{-1}. A Mexican household requires an average of 1.7 to 3.9 MWh yr^{-1} [22], depending on their consumption habits, so one device may supply enough energy for 16 to 38 households. In order to produce a minimum of 1.0 TWh yr^{-1}, a minimum of 15 devices with a 20 m diameter and an efficiency

Preprints (www.preprints.org) | NOT PEER-REVIEWED | Posted: 16 February 2020 doi:10.20944/preprints202002.0216.v1

of at least 35% would be required, conservatively providing enough energy for 240 to 570 households. As the coastal regions are mostly rural, and with poor transmission line development [23], the energy produced should be consumed locally, to reduce costs. A tidal farm with 15 devices would be large enough for that purpose, but it would need to be combined with other energy sources and with energy storage systems.

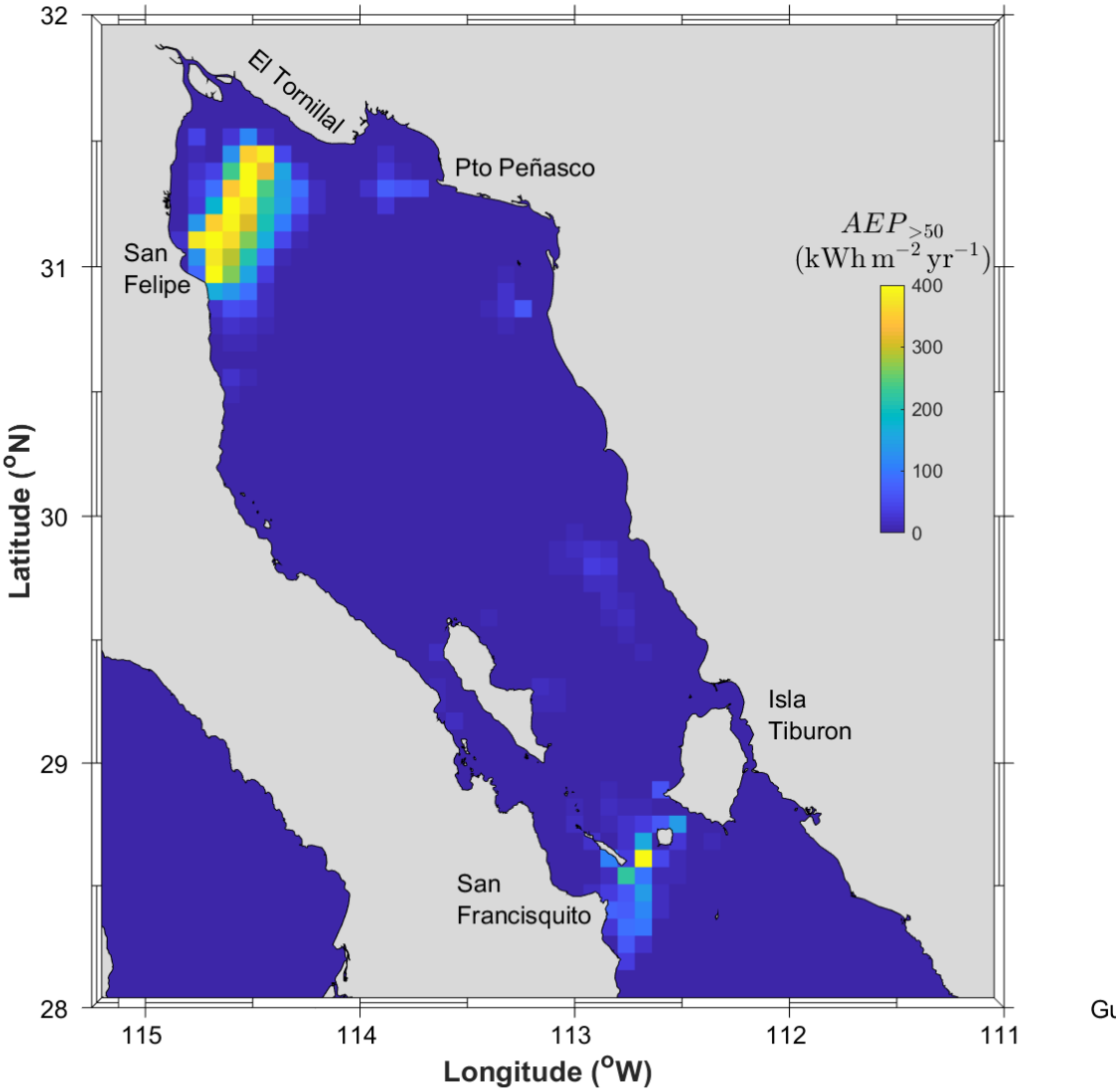

Figure 7. Map of AEP when $TPD > 50$ W m^{-2}.

2.3. Analysis of the wind-driven in-stream energy resource contribution

The plots in Fig. 8 show the residual $\overline{TPD}$ at 0 m, 60 m, 100 m, and 200 m below Mean Sea Level. This residual $\overline{TPD}$ is linked to the wind-driven currents generated by the Navy Global Environmental Model (NAVGEM) forcing. The plots show a region between Mulegé and Guaymas, another region near the southern tip of the Baja California Peninsula, and some locations along the southern transect, joining San Francisquito to Tiburón Island (identified in the barotropic tides analysis), where $\overline{TPD} \approx$ 20 W m^{-2}. From the plots in 8, we deduce that the $\overline{TPD}$ due to the wind forcing is either around or less than 20 W m^{-2}. This is much lower than the economically viable threshold of 50 W m^{-2} assumed earlier. Therefore, these $\overline{TPD}$ values are on their own too low for energy generation, but in locations

Preprints (www.preprints.org) | NOT PEER-REVIEWED | Posted: 16 February 2020 doi:10.20944/preprints202002.0216.v1

where tidal currents are strong, such as in the Punta San Francisquito to Tiburón Island transect, they may play some role in enhancing the tidal energy densities and the annual energy production.

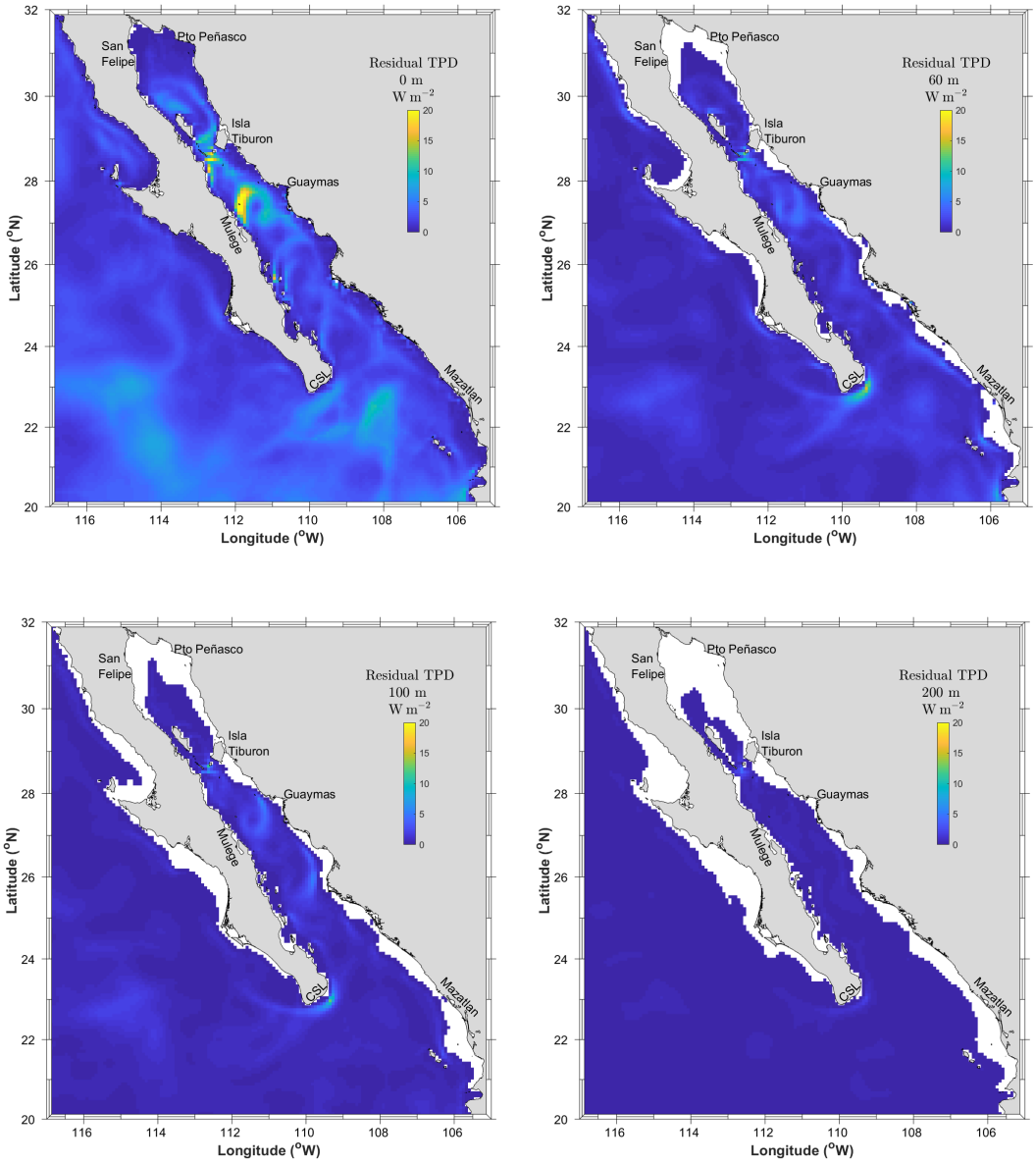

Figure 8. Residual $\overline{TPD}$ at (**a**) 0 m, (**b**) 60 m, (**c**) 100 m, and (**d**) 200 m below Mean Sea Level.

Finally, the plots in Fig. 9 show the relative importance of the AEP produced by the wind-driven currents in relation to the total AEP. The areas where the contribution of the wind-driven current to the total AEP is really small are also areas with large in-stream tidal energy resources, and where discussed in Sec. 2.2. The AEP is dominated by the wind-driven component almost everywhere south of the 28° parallel, except for the region in the Baja Californian Pacific that was briefly mentioned at the end of Sec. 2.2. As the annual $\overline{TPD}$ is less than 20 W m^{-2}, it is not large enough to produce energy by itself. Therefore, the results indicate that the locations for best in-stream energy resource exploitation are still the two transects identified in Sec. 2.2.

Preprints (www.preprints.org) | NOT PEER-REVIEWED | Posted: 16 February 2020 doi:10.20944/preprints202002.0216.v1

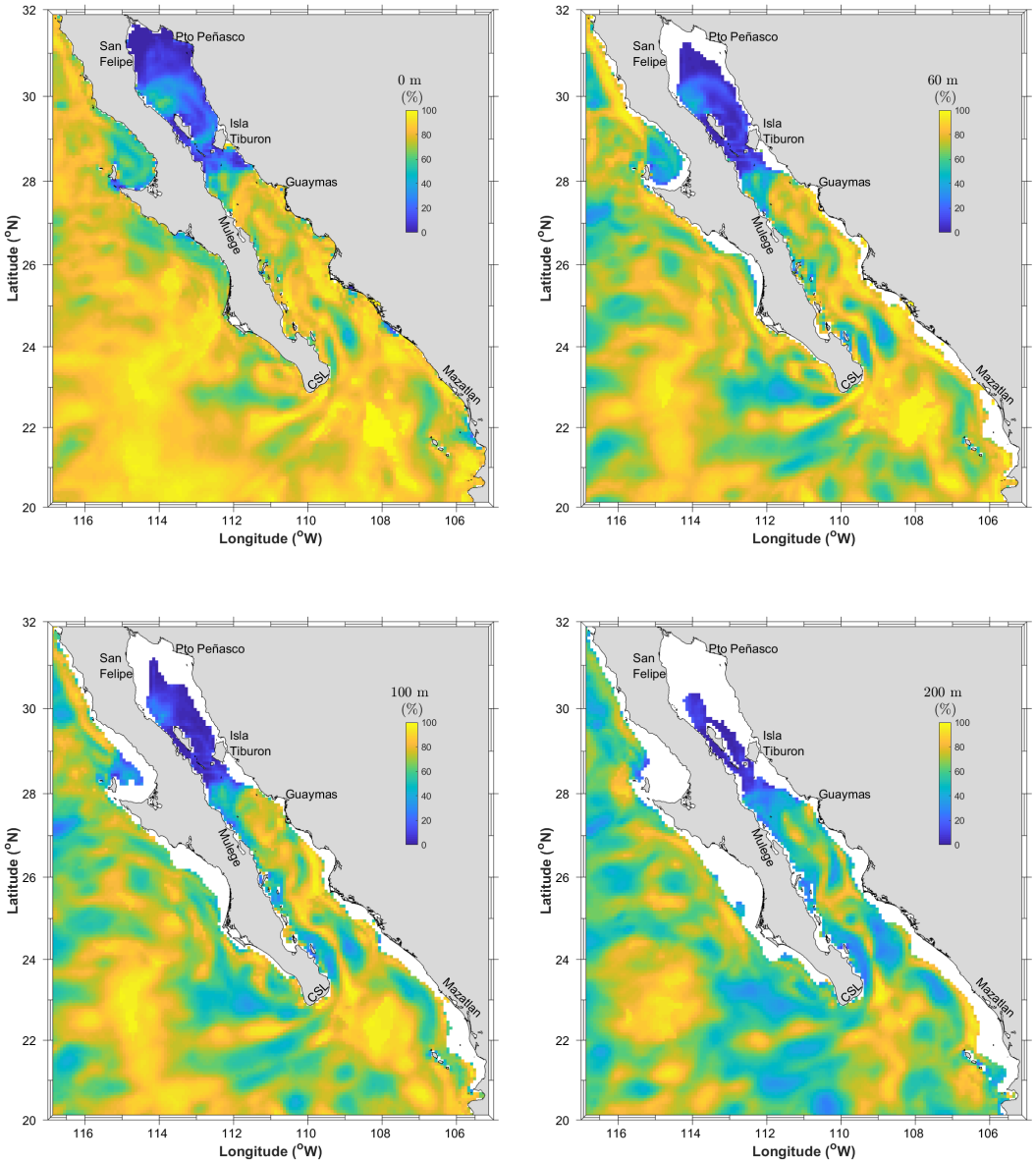

Figure 9. Relative importance of residual AEP against total AEP at 0 m, 60 m, 100 m, and 200 m below Mean Sea Level.

3. Materials and Methods

The "Hybrid Coordinate Ocean Model", referred to as HYCOM since its inception [24], was developed as an outgrowth of the "Miami Isopycnic Coordinate Ocean Model", or MICOM, described in Bleck *et al.* [25]. The model is a primitive equation model with two prognostic equations for the horizontal velocity components (which we express in terms of the velocity vector), one representing the mass continuity or layer-thickness tendency, one for salinity and one for temperature.

The HYCOM experiment we used employs atmospheric forcing from the Navy Global Environmental Model (NAVGEM) [26], and geopotential tidal forcing from the five largest principal tidal components: M_2, S_2, N_2, K_1 and O_1. A self-attraction and load (SAL) term is added to the tidal forcing. The SAL term accounts for the self-gravitation of the tidally deformed ocean and solid earth [27], and for the load deformations of the solid earth [28]. The model has a nominal horizontal resolution of $1/12.5^\circ$ at the equator and 41 isopycnal layers in the vertical. The NAVGEM has a

Preprints (www.preprints.org) | NOT PEER-REVIEWED | Posted: 16 February 2020 doi:10.20944/preprints202002.0216.v1

horizontal resolution of 0.33°, and is interpolated to the finer resolution of the hydrodynamic grid for the simulations. First, the model is run from 1996 to 2003 with a climatological forcing, then from 2003 to 2011 with the atmospheric forcing from the Navy Operational Global Atmospheric Prediction System, NOGAPS [29], and finally, the atmospheric NAVGEM forcing is applied after 30 June 2011. Tidal forcing is initiated on 3 July 2011. Global three-dimensional fields are stored every hour for one year, from 1 October 2011 to 1 October 2012. More details can be found in [30,31].

The analysis is performed over the domain and with the bathymetry shown in Fig. 1, which is the ETOPO1 bathymetry with some sounding corrections in the Great Island Region (GIR) courtesy of CICESE (Zamudio, *pers. comm.*), described in [32]. The GIR moorings were deployed during the "umbrales" (2002-2006) project; these moorings were first reported in [33,34]. The ISJ mooring was deployed between June 2017 and November 2017 during the "CeMIE-Océano" (2017-2021) project, and was first reported in [35].

The in-situ data mentioned above were used to verify the model predictions in the GIR and in ISJ. Since the modelling period extended between 01/10/2011 01:00:00 and 01/10/2012 00:00:00 in hourly timesteps, but the ADCP data were collected at different periods, the verification analysis of the model against the data was performed for the period modelled in the simulations, and focused on the depth-averaged tidal signal alone. The tidal principal component analyses for the ADCP and the simulation results were performed with the T_TIDE tidal analysis package [36], and the tidal signal was reconstructed from the tidal principal components for the simulation period. From this reconstruction, we computed the annual mean tidal speed $\overline{U}$, the annual mean tidal power density $\overline{TPD}$, and the annual energy power AEP:

$$\overline{U} = \frac{1}{N}\sum_{i=1}^{N} U_i, \tag{1}$$

$$\overline{TPD} = \frac{1}{2N}\rho\sum_{i=1}^{N} U_i^3, \text{ and} \tag{2}$$

$$AEP = \frac{1}{2}\rho\sum_{i=1}^{N} U_i^3, \tag{3}$$

with $U_i = \sqrt{u_i^2 + v_i^2}$, $N = 8784$ (2012 is a leap year), and $\rho = 1024\,\mathrm{kg\,m^{-3}}$ is the water density. $\overline{U}$, $\overline{TPD}$, and AEP are computed for the model (mod) and the mooring (obs) data, at each mooring location.

The agreement between model $X = x_{mod}$ and observation $Y = x_{obs}$ was assessed using the Pearson correlation coefficient, $\rho_{X,Y}$, defined as [37]:

$$\rho_{X,Y} = \frac{\mathrm{cov}(X,Y)}{\sigma_X \sigma_Y}, \tag{4}$$

where cov is the covariance between the two time series, and σ_X and σ_Y the standard deviations of X and Y, respectively; the relative error RE_x,

$$RE_x = \left\| \frac{\overline{x}_{obs} - \overline{x}_{mod}}{\overline{x}_{obs}} \right\|; \tag{5}$$

and the root mean square error $RMSE_x$,

$$RMSE_x = \sqrt{\frac{1}{N}\sum_{i=1}^{N} (x_{i,obs} - x_{i,mod})^2}, \tag{6}$$

over the simulation period. Once the model was validated at the mooring locations, we analysed the field maps of $\overline{U}$, $\overline{TPD}$, and AEP, as well as the annual means of the spring tide maxima, $\overline{U}_{STM}$ and $\overline{TPD}_{STM}$, to determine the best sites for tidal and wind-driven current energy extraction, based on $\overline{U}$, $\overline{TPD}$, and AEP. We also assessed the percentage contribution of each of them throughout the case

study domain, and discuss some implications for tidal and wind-driven current power generation. It is worth noting that here we will not consider any techo-economic or socio-ecological constraints, but the analysis would be similar to that for wind energy resource characterization studies developed in previous work [23,38].

4. Conclusions

A tide and wind-driven shallow water global model was used to make a mesoscale evaluation of in-stream renewable energy resources in the Gulf of California and the Baja Californian Pacific. The region is characterized by low current speeds, relative to regions that are adequate for first generation in-stream energy devices. With this model, some regions within the Gulf of California with mean annual tidal power densities between 141 and 173 W m^{-2} during energy producing periods were identified. The tides would be producing energy at these sites for around 31% to 39% of the time, when assuming that second to fifth generation technologies can generate electricity at this minimum TDP threshold. The in-stream energy resources are strongly dominated by the tidal stream component, with wind-driven currents generating TPD generally below 20 W m^{-2}. The installation of 15 devices with a diameter of 20 m and an efficiency of 35% would provide enough energy for 240 to 570 households. These devices could be installed along two transects, either between San Felipe and El Tornillal in the Upper Gulf of California, or between San Francisquito and Tiburón Island, in the Great Island Region.

Author Contributions: conceptualization, VM and MSG; methodology, VM and LZ; software, LZ; validation, MLM and VMG; formal analysis, VM; data curation, ABR, MLM and VMG; resources, JC; writing–original draft preparation, VM; writing–review and editing, all authors; visualization, VMG and VM; project administration, VM; funding acquisition, VM.

Funding: This work was partially supported by the SENER-CONACYT grant no. 249795, within the project "CeMIE-Océano" (2017-2021).

Acknowledgments: Thanks to the Department of Physical Oceanography of CICESE, and in particular technician Erick Rivera-Lemus, for his support with fieldwork and data acquisition. Thanks to the waves group of CICESE (led by Dr. Paco Ocampo), for support with technician time and batteries provided for instrumentation. Thanks to the Oceanographic Equipment Coordination and the CANEK group of CICESE, for support with equipment and equipment maintenance resources. HYCOM simulation was performed on the Navy Department of Defense (DoD) Supercomputing Resources at Stennis Space Center, Mississippi, using grants of computer time from the DoD High Performance Computing Modernization Program.

Conflicts of Interest: The authors declare no conflict of interest. The funders had no role in the design of the study; in the collection, analyses, or interpretation of data; in the writing of the manuscript, or in the decision to publish the results.

Abbreviations

The following abbreviations are used in this manuscript:

TPD	Tidal Power Density
AEP	Annual Energy Production

References

1. Parker, B.B., Ed. *Tidal Hydrodynamics*; Wiley, 1991.
2. Dupont, F.; Hannah, C.G.; Greenberg, D. Modelling the sea level of the upper Bay of Fundy. *Atmosphere-Ocean* **2005**, *43*, 33–47. doi:10.3137/ao.430103.
3. Hiriart Le Bert, G. Potencial energético del Alto Golfo de California. *Boletín de la Sociedad Geológica Mexicana* **2009**, *61*, 143–146. doi:10.18268/bsgm2009v61n1a13.
4. Xia, J.; Falconer, R.A.; Lin, B. Hydrodynamic impact of a tidal barrage in the Severn Estuary, UK. *Renewable Energy* **2010**, *35*, 1455–1468. doi:10.1016/j.renene.2009.12.009.
5. Carbajal, N.; Backhaus, J.O. Simulation of tides, residual flow and energy budget in the Gulf of California. *Oceanologica Acta* **1998**, *21*, 429–446. doi:10.1016/s0399-1784(98)80028-5.
6. Garrett, C.; Cummins, P. The power potential of tidal currents in channels. *Proceedings of the Royal Society A: Mathematical, Physical and Engineering Sciences* **2005**, *461*, 2563–2572. doi:10.1098/rspa.2005.1494.

7. Defne, Z.; Haas, K.A.; Fritz, H.M. Numerical modeling of tidal currents and the effects of power extraction on estuarine hydrodynamics along the Georgia coast, USA. *Renewable Energy* **2011**, *36*, 3461–3471. doi:10.1016/j.renene.2011.05.027.
8. Yang, X.; Haas, K.A.; Fritz, H.M. Theoretical Assessment of Ocean Current Energy Potential for the Gulf Stream System. *Marine Technology Society Journal* **2013**, *47*, 101–112. doi:10.4031/mtsj.47.4.3.
9. Perez-Collazo, C.; Pemberton, R.; Greaves, D.; Iglesias, G. Monopile-mounted wave energy converter for a hybrid wind-wave system. *Energy Conversion and Management* **2019**, *199*, 111971. doi:10.1016/j.enconman.2019.111971.
10. Dalton, G.; Bardócz, T.; Blanch, M.; Campbell, D.; Johnson, K.; Lawrence, G.; Lilas, T.; Friis-Madsen, E.; Neumann, F.; Nikitas, N.; Ortega, S.T.; Pletsas, D.; Simal, P.D.; Sørensen, H.C.; Stefanakou, A.; Masters, I. Feasibility of investment in Blue Growth multiple-use of space and multi-use platform projects; results of a novel assessment approach and case studies. *Renewable and Sustainable Energy Reviews* **2019**, *107*, 338–359. doi:10.1016/j.rser.2019.01.060.
11. Tweed, K. Underwater Kite Harvests Energy From Slow Currents – Could kites be the secret to capturing tidal energy?, 2013. Last accessed: 19/11/2019.
12. Minesto. https://www.minesto.com/our-technology, 2019. Last accessed: 19/11/2019.
13. Magar, V. Tidal Current Technologies. In *Sustainable Energy Technologies*; CRC Press, 2017; pp. 293–308. doi:10.1201/9781315269979-18.
14. Byrne, J.V.; Emery, K.O. Sediments of the Gulf of California. *Geological Society of America Bulletin* **1960**, *71*, 983. doi:10.1130/0016-7606(1960)71[983:sotgoc]2.0.co;2.
15. Morales Pérez, R.A.; Gutiérrez de Velazco Sanromán, G. Mareas en el Golfo de California. *Geofísica Internacional* **1989**, *28*, 25 – 46.
16. Álvarez, L.G.; Suárez-Vidal, F.; Mendoza-Borunda, R.; González-Escobar, M. Bathymetry and active geological structures in the Upper Gulf of California. *Boletín de la Sociedad Geológica Mexicana* **2009**, *61*, 129 – 141.
17. Corsatea, T.D.; Magagna, D. Overview of European innovation activities in marine energy technology. Technical report, Environmental Sciences Group, Brussels, BE, 2014.
18. Verdant Power. Technology Advancement, 2019. Last accessed: 21/11/2019.
19. LeGrand, C. Assessment of Tidal Energy Resource – Marine Renewable Energy Guides. Technical report, Black and Veatch Ltd, London, UK, 2009.
20. Myers, L.; Bahaj, A. Power output performance characteristics of a horizontal axis marine current turbine. *Renewable Energy* **2006**, *31*, 197–208. doi:10.1016/j.renene.2005.08.022.
21. Iyer, A.; Couch, S.; Harrison, G.; Wallace, A. Variability and phasing of tidal current energy around the United Kingdom. *Renewable Energy* **2013**, *51*, 343–357. doi:10.1016/j.renene.2012.09.017.
22. Oropeza-Perez, I.; Petzold-Rodriguez, A. Analysis of the Energy Use in the Mexican Residential Sector by Using Two Approaches Regarding the Behavior of the Occupants. *Applied Sciences* **2018**, *8*, 2136. doi:10.3390/app8112136.
23. Magar, V.; Gross, M.; González-García, L. Offshore wind energy resource assessment under techno-economic and social-ecological constraints. *Ocean & Coastal Management* **2018**, *152*, 77–87. doi:10.1016/j.ocecoaman.2017.10.007.
24. Bleck, R. An oceanic general circulation model framed in hybrid isopycnic-Cartesian coordinates. *Ocean Modelling* **2002**, *4*, 55–88. doi:10.1016/s1463-5003(01)00012-9.
25. Bleck, R.; Rooth, C.; Hu, D.; Smith, L.T. Salinity-driven Thermocline Transients in a Wind- and Thermohaline-forced Isopycnic Coordinate Model of the North Atlantic. *Journal of Physical Oceanography* **1992**, *22*, 1486–1505. doi:10.1175/1520-0485(1992)022<1486:sdttia>2.0.co;2.
26. Hogan, T.F.; Liu, M.; Ridout, J.A.; Peng, M.S.; Whitcomb, T.R.; Ruston, B.C.; Reynolds, C.A.; Eckermann, S.D.; Moskaitis, J.R.; Baker, N.L.; McCormack, J.P.; Viner, K.C.; Mclay, J.G.; Flatau, M.K.; Xu, L.; Chen, C.; Chang, S.W. The Navy Global Environmental Model. *Oceanography* **2014**, *27*, 116–125.
27. Ray, R.D. Ocean self-attraction and loading in numerical tidal models. *Marine Geodesy* **1998**, *21*, 181–192. doi:10.1080/01490419809388134.
28. Hendershott, M.C. The Effects of Solid Earth Deformation on Global Ocean Tides. *Geophysical Journal International* **1972**, *29*, 389–402. doi:10.1111/j.1365-246x.1972.tb06167.x.

29. Rosmond, T.; Teixeira, J.; Peng, M.; Hogan, T.; Pauley, R. Navy Operational Global Atmospheric Prediction System (NOGAPS): Forcing for Ocean Models. *Oceanography* **2002**, *15*, 99–108. doi:10.5670/oceanog.2002.40.
30. Buijsman, M.C.; Arbic, B.K.; Richman, J.G.; Shriver, J.F.; Wallcraft, A.J.; Zamudio, L. Semidiurnal internal tide incoherence in the equatorial Pacific. *Journal of Geophysical Research: Oceans* **2017**, *122*, 5286–5305. doi:10.1002/2016jc012590.
31. Arbic, B.K.; Alford, M.H.; Ansong, J.K.; Buijsman, M.C.; Ciotti, R.B.; Farrar, J.T.; Hallberg, R.W.; Henze, C.E.; Hill, C.N.; Luecke, C.A.; Menemenlis, D.; Metzger, E.J.; Müeller, M.; Nelson, A.D.; Nelson, B.C.; Ngodock, H.E.; Ponte, R.M.; Richman, J.G.; Savage, A.C.; Scott, R.B.; Shriver, J.F.; Simmons, H.L.; Souopgui, I.; Timko, P.G.; Wallcraft, A.J.; Zamudio, L.; Zhao, Z. A Primer on Global Internal Tide and Internal Gravity Wave Continuum Modeling in HYCOM and MITgcm. In *New Frontiers in Operational Oceanography*; GODAE OceanView, 2018. doi:10.17125/gov2018.ch13.
32. Argote, M.L.; Amador, A.; Lavín, M.F.; Hunter, J.R. Tidal dissipation and stratification in the Gulf of California. *Journal of Geophysical Research* **1995**, *100*, 16103. doi:10.1029/95jc01500.
33. López, M.; Candela, J.; Argote, M.L. Why does the Ballenas Channel have the coldest SST in the Gulf of California? *Geophysical Research Letters* **2006**, *33*. doi:10.1029/2006gl025908.
34. López, M.; Candela, J.; García, J. Two overflows in the Northern Gulf of California. *Journal of Geophysical Research* **2008**, *113*. doi:10.1029/2007jc004575.
35. Bermúdez-Romero, A.; Magar, V.; Gross, M.S.; Godínez, V.M.; López-Mariscal, M.; Rivera-Lemus, E. Characterization of in-stream tidal energy resources in the Gulf of California: implementation, calibration and validation of a hydrodynamic model. Proceedings of the 13^{th} European Wave and Tidal Energy Conference (EWTEC2019), Napoli, Italy, 2019, European Wave and Tidal Energy Conference Series.
36. Pawlowicz, R.; Beardsley, B.; Lentz, S. Classical tidal harmonic analysis including error estimates in MATLAB using T_TIDE. *Computers & Geosciences* **2002**, *28*, 929–937. doi:10.1016/s0098-3004(02)00013-4.
37. Pearson, K. Mathematical Contributions to the Theory of Evolution. III. Regression, Heredity, and Panmixia. *Philosophical Transactions of the Royal Society A: Mathematical, Physical and Engineering Sciences* **1896**, *187*, 253–318. doi:10.1098/rsta.1896.0007.
38. Magar, V.; González-García, L.; Gross, M.S. Evaluación Técnico-económica del Potencial de Desarrollo de Parques Eólicos en Mar: El Caso del Golfo de California. *BIOtecnia* **2017**, *19*, 3–8. doi:10.18633/biotecnia.v19i0.358.